Biosensors and Bioelectronics 141 (2019) 111444

Contents lists available at ScienceDirect

Biosensors and Bioelectronics

journal homepage: www.elsevier.com/locate/bios

Building electrode with three-dimensional macroporous interface from biocompatible polypyrrole and conductive graphene nanosheets to achieve highly efficient microbial electrocatalysis

Liming Yang[a], Genping Yi[a], Yanan Hou[d], Haoyi Cheng[b], Xubiao Luo[a], Spyros G. Pavlostathis[c], Shenglian Luo[a,*], Aijie Wang[b,**]

[a] Key Laboratory of Jiangxi Province for Persistent Pollutants Control and Resources Recycle, Nanchang Hangkong University, Nanchang, 330063, PR China
[b] Key Laboratory of Environmental Biotechnology, Research Center for Eco-Environmental Sciences, Chinese Academy of Sciences, Beijing, 100085, PR China
[c] School of Civil and Environmental Engineering, Georgia Institute of Technology, Atlanta, GA, 30332-0512, United States
[d] China Tianjin Key Laboratory of Aquatic Science and Technology, School of Environmental and Municipal Engineering, Tianjin Chengjian University, Jinjing Road 26#, Tianjin, 300384, PR China

ARTICLE INFO

Keywords:
Microbial electrocatalysis
Electrode interface
Graphene
Polypyrrole
Microbial colonization
Electron transfer

ABSTRACT

Bioelectrochemical systems (BESs) possess a great potential for simultaneous wastewater treatment and energy recovery. Rational construction of electrode materials could significantly improve the BESs performance. Three-dimensional macroporous electrode interface with high conductivity is highly desirable but challenging. In this work, we report a hierarchically nanostructured reduced graphene oxide nanosheets-polypyrrole (rGO@PPy) electrode *via* one-step electrodeposition technique. The prepared electrode was comprehensively studied by scanning/transmission electron microscopy, Raman spectroscopy, X-ray diffraction and electrochemical measurements, which showed that the rGO@PPy possessed a three-dimensional macroporous interconnecting scaffold with superior conductivity. The rGO@PPy electrode was utilized in *Geobacter sulfurreducens* inoculated BESs, and the maximum current density was 4.10 ± 0.02 mA cm^{-2}, which is 8-fold higher than that of a rGO electrode (0.51 ± 0.03 mA cm^{-2}), and is among the best performance reported for two-dimensional electrodes. The improved performance is ascribed to ultrahigh biomass concentration induced by "best match scale" between rGO@PPy and microbes, excellent extracellular electron transfer, as well as enhanced microbial affinity through the adequate exposure of biocompatible PPy layers. This work demonstrated a synergistic effect between rGO and PPy for the BESs performance improvement, and provided a new insight to design and fabricate a high-performance bioelectrode.

1. Introduction

Bioelectrochemical systems (BESs) have been demonstrated as an innovative, sustainable and efficient technology for wastewater treatment, electricity or hydrogen generation, bioremediation, biosensors, etc. [Logan et al., 2006; Logan et al., 2012]. To increase the efficiency of the systems, extensive efforts have been made in electroactive microbial analysis [Kumar et al., 2016; Liang et al., 2019], bioelectrochemical reactor design, and electrode materials [Sun et al., 2016; Yang et al., 2019]. It has been found that the core component is the electroactive biofilms (EABs) [Kumar et al., 2017], which play a crucial role in determining the system performance [Katuri et al., 2018; Aryal et al., 2017]. In view of this, various electrode materials have been developed to increase biofilm formation, including biocompatible surface decoration and three-dimensional macroporous electrode construction with enhanced surface areas. Xie et al. [Xie et al., 2015] summarized different kinds of electrode materials for BESs, varying from nonporous bulk electrodes to fiber-based, particle-based and monolithic porous electrodes. Despite remarkable improvements have been achieved, low biomass loading onto the electrode and inferior extracellular electron transfer (EET) efficiency between bacteria and electrodes are still major bottlenecks that limit the practical application of BESs [Zhao et al., 2009].

Carbon-based materials, such as carbon cloth, carbon paper, carbon fiber, and granular activated carbon, have been widely used as anodes for the enrichment of EABs [S. Li et al., 2017; Cui et al., 2018].

* Corresponding author.
** Corresponding author.
E-mail addresses: sllou@hnu.edu.cn (S. Luo), ajwang@rcees.ac.cn (A. Wang).

https://doi.org/10.1016/j.bios.2019.111444
Received 30 January 2019; Received in revised form 7 June 2019; Accepted 15 June 2019
Available online 16 June 2019
0956-5663/ © 2019 Elsevier B.V. All rights reserved.

However, these carbon-based electrodes usually suffer from inferior EET efficiency and weak microbial affinity [Tao et al., 2016; Chaudhuri et al., 2003]. More importantly, the obtained biomass per unit electrode area is too low as the pores of the materials are either too small or too large [Zou et al., 2017; Jiang et al., 2017; Song et al., 2016]. An effective combination of hierarchical pore structures (macro-, meso- and micro-based pores) is necessary [Hochbaum et al., 2010; Ye et al., 2017; Massazza et al., 2018; Yu et al., 2019]. Graphene, a 2D aromatic monolayer of carbon, shows great potential in BES applications by taking advantage of its extremely high specific surface area and outstanding electrical conductivity [Liu et al., 2012; Yuan et al., 2015; Mashkour et al., 2017]. Nevertheless, when serving as electrode material, the electrochemical performance of graphene was severely limited due to its strong irreversible aggregation. In this regard, hybridization with other electrochemically active moieties has been considered good alternatives to establish stable sandwich-like structures [Liu et al., 2011]. Conducting polymers, such as polypyrrole (PPy), have drawn specific attention in electrode modification owing to its high biocompatibility, low cost and adjustable redox potential [Song et al., 2017]. The combination of graphene and conducting polymers was achieved to improve the performance of the BESs [Yong et al., 2012; Hou et al., 2013; Min et al., 2019; ElMekawy et al., 2017], however, no comprehensive study has been conducted to investigate the effect of pore size distribution and microstructure properties on the bioelectrocatalytic performance of BESs. Therefore, it is highly desirable to optimize the chemical structure and surface functionality of graphene-conducting polymers to realize excellent conductivity and biocompatibility for fast microbial adhesion/colonization, thus enhancing BES performance.

In this work, we designed and fabricated a hierarchically structured reduced graphene oxide-polypyrrole (rGO@PPy) nanohybrid and used it as a BES electrode. The objectives of this study were to (i) get the "best match scale" between electrode nanomaterials and microbes; (ii) increase the EET efficiency by improving the electrode conductivity; and (iii) enhance the microbial affinity by the PPy introduction. The hierarchical rGO@PPy electrode exhibits an open porous and three-dimensional interconnecting conductive scaffold with higher surface roughness, facilitating EET and microbial colonization.

2. Experimental section

2.1. Chemicals and materials

Pyrrole (Py) was purchased from Sinopharm Chemical Reagent (Beijing, China) and distilled twice under reduced pressure prior to use. Lithium perchlorate ($LiClO_4$) and other chemicals were commercially available analytical grade reagents (Beijing Chemical Reagent Co., Ltd., Beijing, China), and used directly without further purification. Ultrapure water (18.2 MΩ-cm at 25 ± 1 °C) was obtained using a Milli-Q/Millipore water purification system.

2.2. Preparation of rGO@PPy electrode

Graphite oxide powder was prepared using a previously-reported improved method [L. Yang et al., 2015], and then exfoliated in a 0.1 M $LiClO_4$ solution by ultrasonication for 3 h to form 0.5 g L^{-1} graphene oxide (GO) colloidal suspension. Afterwards, Py monomer was added into the above GO suspension at a volume ratio of V_{Py}:V_{GO} = 1:2000. Then, cyclic voltammetric (CV) electrodeposition was conducted using a CHI 660C electrochemical workstation (CH Instruments, Shanghai, China) with three-electrode mode: a glassy carbon electrode (GCE, 4 mm in diameter, 0.1256 cm^2) served as the working electrode, a saturated Ag/AgCl reference electrode, and a Pt mesh (1.0 cm^2 in geometric area) used as the counter electrode. The scan range was between −1.5 V and 0.9 V *vs.* Ag/AgCl with a rate of 50 mV s^{-1} for 20 cycles. After the electrodeposition, the electrode was rinsed with ultrapure water and dried at room temperature (25 ± 1 °C) for use. Using the same method, pure rGO film was obtained from 0.5 g L^{-1} GO, and pure PPy film was obtained from 0.1 M $LiClO_4$ solution containing Py (V_{Py}:V_{LiClO4} = 1:2000).

2.3. Preparation of biofilm on electrode surface

Geobacter sulfurreducens PCA (DSM 12127) was used as the electroactive bacterium, pre-cultured in PCA standard medium with fumarate as the electron acceptor [Hou et al., 2016; Reguera et al., 2005]. Eight identical GCEs (4.0 mm in diameter) separately served as working electrodes, which shared one saturated Ag/AgCl reference electrode and one Pt mesh (1.0 cm^2 in geometric area) as the counter electrode (Fig. S1). PCA standard medium (without fumarate due to electrode acting as electron acceptor) was used as growth medium, flushed with N_2/CO_2 (v/v = 80/20) for 30 min and sterilized by autoclaving. The activated *Geobacter* suspensions with OD_{600} of 0.3–0.5 were then added into the electrochemical cell (Fig. S1) containing the pretreated PCA standard medium. Sodium acetate (1.0 g L^{-1}) was added and served as carbon and electron source. For bacterial biofilm growth, the potentials of the working electrodes (rGO@PPy, rGO and bare GCE) were poised at 0 V *vs.* Ag/AgCl, and the current was recorded over time. All reported data are based on at least three independent replicates with each of the electrode materials.

The biofilm biomass was estimated from the amount of total protein on the electrode, as follows. The electrodes were dispersed in 1.0 M NaOH solution at 40 °C for 12 h to fully dissolve the cells. Protein measurements were performed with Micro BCA Protein Assay Kit (Sangon Biotech Co., China) according to manufacturer's instructions. Bovine serum albumin was used as the standard for quantification [D. B. Li et al., 2017].

2.4. Physical characterization

The morphologies of the electrode materials were characterized by field emission-scanning electron microscopy (SEM, Hitachi, SU8000) and transmission electron microscopy (TEM, FEI Tecnai G^2 F30 S-TWIN) equipped with an energy dispersive X-ray spectrometer (EDX). The morphologies of the biofilms were also characterized by SEM. Prior to the SEM observation, the bioelectrodes were fixed for 1.5 h in 2.5% glutaraldehyde, washed three times with 0.1 M phosphate buffered solution, sequentially dehydrated with increasing concentrations of ethanol solution (25, 50, 70, 80, 90, and 100%), dried overnight and then coated with Au. X-ray diffraction (XRD) patterns were performed on an X-ray diffractometer (Bruker D8 Advance, Germany) using Cu Kα radiation (λ = 0.15406 nm) at a power of 40 keV and 3 × 30 mA. Raman spectra were recorded from 500 to 3500 cm^{-1} using an Advantage 200A Raman spectrometer with a 632.8 nm laser (DeltaNu, USA). N_2 adsorption-desorption isotherms were obtained at 77 K with Micromeritics TriStar II 3020 (USA) after dehydration under vacuum at 473 K for 4 h. The meso- and micro-pore size distribution was analyzed based on the Barrett-Joyner-Halenda (BJH) adsorption model according to the desorption branch of the isotherm, and the macro-pore size was determined using mercury porosimetry. The stained cells were examined using a Leica TCS SP5 II confocal laser scanning microscope (CLSM, Germany). Zeta potential charge of different electrode materials was measured with a Nano ZS90 Zeta potential analyzer (Malvern, UK).

2.5. Electrochemical measurements

Electrochemical measurements were performed on a standard three-electrode system using an electrochemical workstation (CHI 1000). Bare GCE, rGO, PPy and rGO@PPy were used as the working electrodes, and Pt mesh (1.0 cm^2 in geometric area) and saturated Ag/AgCl were used as the counter electrode and the reference electrode, respectively. Cyclic voltammograms (CVs) were obtained by scanning

the potential from −0.4 V to 0.6 V in N_2-saturated 1.0 M KCl solution at a scan rate of 50 mV s^{-1}. Electrochemical impedance spectra (EIS) were recorded by applying an AC voltage with 5 mV amplitude over a frequency range of 0.01–100000 Hz at 0 V *vs*. saturated Ag/AgCl electrode. Linear sweep voltammetry (LSV) curves were obtained from −0.6 V to 0.6 V at a scan rate of 10 mV s^{-1}.

3. Results and discussion

3.1. rGO@PPy synthesis and morphological characterization

The rGO@PPy hybrid was synthesized by the one-step electrodeposition method with GO and Py as the starting materials (Fig. S2). The electrodeposition technique is simple, rapid, green and suitable for synthesizing "clean" electrode materials without additional chemical binders. Because rGO nanosheets can be obtained *via* GO electro-reduction and PPy can be prepared by Py monomer electro-oxidation, the CV method was used for the electrochemical preparation of the rGO@PPy hybrid (Fig. S3a). According to our previous works [Yang et al., 2014; L. M. Yang et al., 2015], hierarchically nanostructured rGO@PPy can be obtained by tuning the concentration ratios of Py to GO. As shown in Fig. 1a, the as-prepared rGO@PPy hybrid shows an ordered 3D cross-linked structure with hierarchical pore sizes. The enlarged SEM image (Fig. 1b) suggests that the hybrid consists of multiple layers of nanosheets and pore structures of different sizes (including macro-, meso- and micro-pores). The rGO surface was covered by PPy layer, which was confirmed by TEM characterization as discussed below. The individual rGO and PPy were also prepared through the same CV electrodeposition (Figs. S3b and c). In contrast, the obtained rGO (Fig. 1c) and PPy (Fig. 1d) were compacted, and totally different from the 3D rGO@PPy nanostructure, which is not beneficial to bacterial attachment and growth.

The TEM technique was used to characterize the microstructure of the rGO@PPy hybrid. Fig. 2a shows that the formed nanosheets interact with each other. The enlarged TEM image (Fig. 2b) reveals that the obtained sheets were decorated by thin PPy layer, and a sandwich-like structure was formed with rGO nanosheet inserted in the middle. That is to say, the graphene layer is shielded by the PPy layer, which would protect exoelectrogenic bacteria from the antibacterial effect of graphene [Chen et al., 2015]. EDX results (Fig. S4) show that the hybrid consists of three different elements (C, 67.29 *w.t.*%; N, 10.08 *w.t.*%; and O, 22.63 *w.t.*%), which are homogeneously distributed on the single nanosheet (Fig. 2c, d and e). Compared to traditional carbon materials, the high content of N atoms introduced by PPy could substantially increase electrode biocompatibility [Ci et al., 2012; Wei et al., 2016; Yang et al., 2016]. XRD pattern further confirmed the formation of rGO@PPy hybrid (Fig. 2f). The large C(002) peak is attributed to the presence of graphene and the peaks marked by black squares are ascribed to the characteristic peaks of PPy. Raman spectrum (Fig. 2g) shows peaks of D, G, 2D and D + G, which are attributed to rGO. The larger G peak than D peak indicates that the obtained rGO possesses intact sp^2 hybridized atomic structure. Five peaks at 924, 983, 1054, 1245, and 1480 cm^{-1} are assigned to PPy [Ren et al., 2015; Liu et al., 2017; Shao et al., 2019]. These results indicate that the hybrid was composed of rGO and PPy, and their combination would be conducive to enhanced microbial electrocatalytic performance.

3.2. Electrochemical measurements

The typical Nyquist plots recorded for the three electrodes are presented in Fig. 3a. The diameter of the semicircles are related to the charge transfer resistance. The smaller the diameter of the semicircles, the lower the charge transfer resistance (R_{ct}) and the higher the conductivity. It can be seen that the R_{ct} of the rGO@PPy electrode is much lower than for the others (detailed resistance values are shown in Table S1). Furthermore, the conductivity was evaluated through CV in N_2-saturated potassium ferrocyanide solution at a scan rate 50 mV s^{-1} (Fig. S5). Results show that the PPy possesses inferior conductivity, which is far worse than that of rGO, and even worse than that of bare GCE. Considering the influence of bulk electrolyte solution, the conductivity

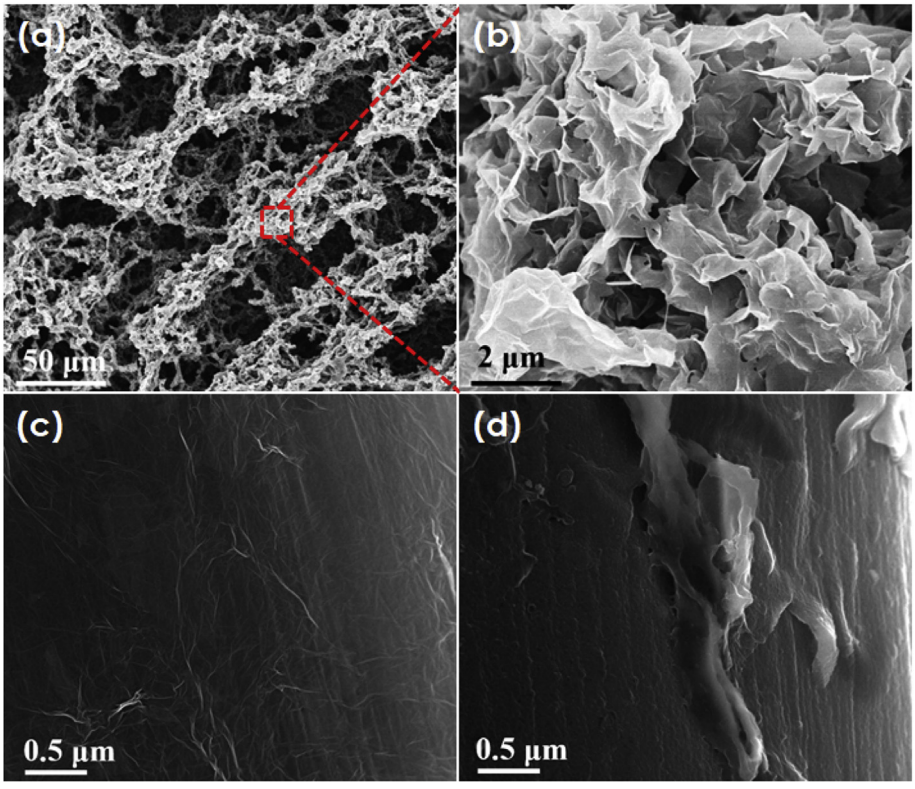

Fig. 1. SEM images of (a, b) hierarchically nanostructured rGO@PPy, (c) rGO and (d) PPy.

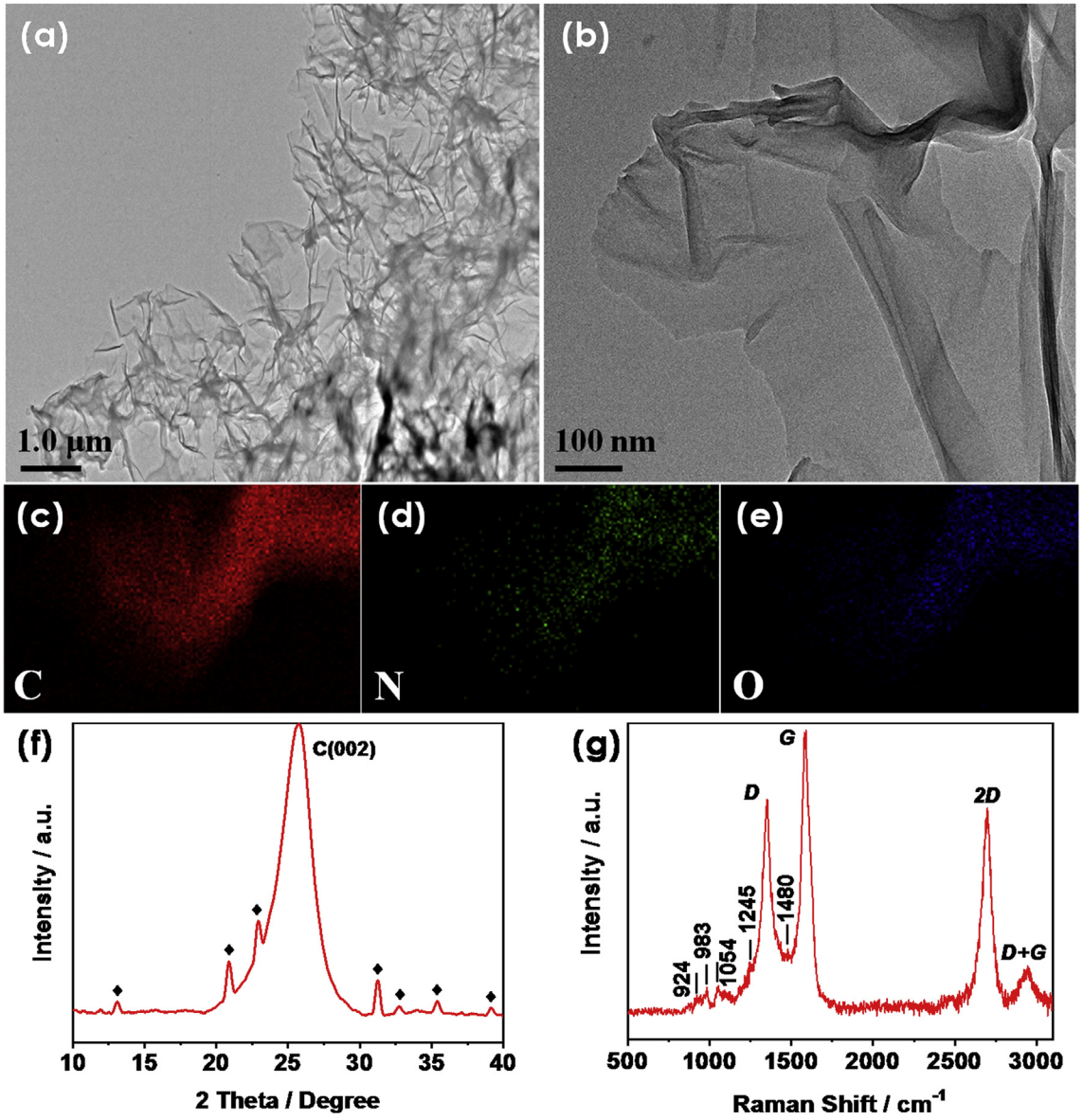

Figure 2. (a, b) TEM images of rGO@PPy hybrid; corresponding elemental mapping of C (c), N (d) and O (e); XRD pattern (f) and Raman spectrum (g) of rGO@PPy hybrid.

was also measured through *I-V* curves using an on-chip microelectrode (the image is shown in Fig. S6). The conductivity of PPy was so low that could not be recorded. The slope value of the *I vs. V* line with the rGO@PPy electrode is much higher than with the rGO (Fig. 3b), further indicating that rGO@PPy possesses a better conductivity. The excellent conductivity of rGO@PPy hybrid would facilitate EET between the bacteria and the electrode.

The electrochemical surface areas (ECSAs) were compared using CV. All voltammograms show a quasi-rectangular shape due to the electric double-layer capacitance. As expected, the highest area of CV curve was observed with the rGO@PPy hybrid (Fig. 3c), indicating that the ECSA value of the rGO@PPy hybrid is much larger than that of rGO. From Fig. 3d, rGO shows the largest CV integral area, and the ECSA value of rGO is much larger than that of PPy and bare electrode. It should be noted that the rGO@PPy hybrid possesses a pair of reversible redox peaks centered at 0.3 V, which is the pseudocapacitance effect from Faradaic redox reactions of PPy [Lin et al., 2015; Ding et al., 2016]. This phenomenon could favor the acceptance and storage of electrons from the electrogenic bacteria [Yong et al., 2012; Zhang et al., 2016]. In addition, the ECSA value of PPy is even smaller than that of the bare electrode. However, once a small amount of PPy was added, the microbial electrocatalytic performance was greatly improved, which demonstrates that the PPy mainly contributes to the electrode biocompatibility. The large surface area is not necessary to improve the performance of bioelectrodes, but instead the pore size distribution is very important, as it is related to molecular diffusion and microbial colonization and growth. The plot of pore size distribution based on the BJH model is shown in Fig. 3e; many meso- and micro-pores were observed, which is beneficial to mass transfer of nutrients. The macro-pore size distribution curve based on mercury porosimetry is shown in Fig. 3f. The macro-pore distribution is centered at about 100 μm; the macroporous features are beneficial for microbial attachment and growth [Jiang et al., 2017; You et al., 2016; Bian et al., 2018]. These results indicate that the unique scaffold of the rGO@PPy electrode has a large surface-area and proper pore size distribution, thus providing more compatible sites for bacteria attachment and growth, as well as facilitating nutrient diffusion from the bulk solution to the electrode interior.

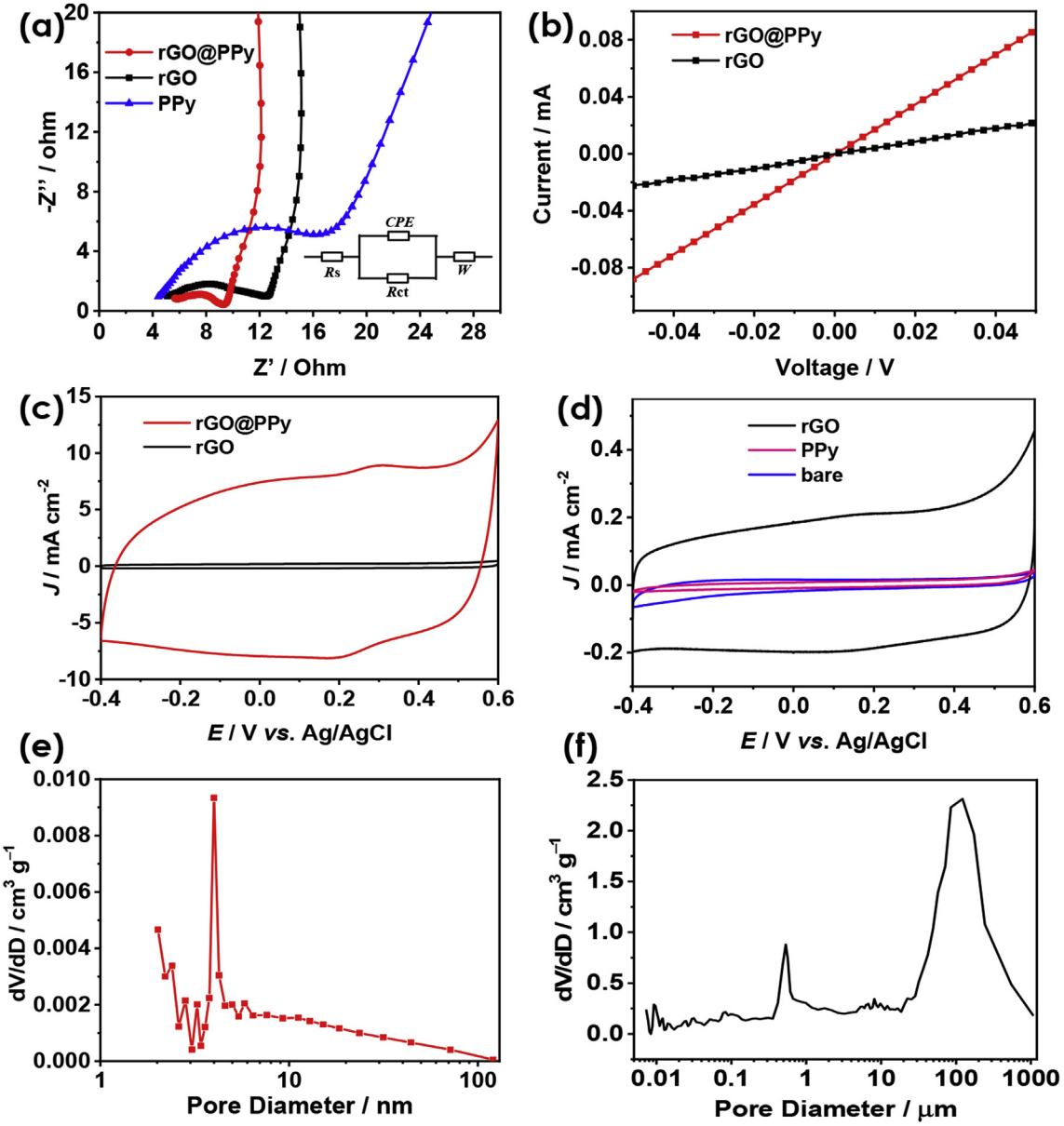

Figure 3. (a) Nyquist plots for rGO@PPy, rGO and PPy modified electrodes measured over a frequency range of 0.01–100000 Hz with an AC perturbation of 5 mV (the inset is equivalent circuit used for fitting the impedance data); (b) Current *vs.* voltage (*I-V*) measurements of rGO@PPy (red) and rGO (black) using the on-chip microelectrode (interspacing: 0.12 mm); (c, d) CVs of rGO@PPy, rGO, PPy and bare electrode in N_2-saturated 1.0 M KCl solution at a scan rate of 50 mV s^{-1}; (e) BJH pore size distribution curve of rGO@PPy; (f) Macro-pore size distribution curve based on mercury injection porosimetry.

3.3. Microbial electrocatalytic performance

The microbial electrochemical characteristics of the rGO@PPy hybrid were investigated in a single-chamber BES with *Geobacter* inoculation. The bioelectrocatalytic current generation with the rGO@PPy and bare electrodes is presented in Fig. 4a. The maximum current density of rGO@PPy was as high as 4.10 ± 0.02 mA cm^{-2} (normalized to the electrode projected area, similarly hereinafter), which is much higher than that of the bare electrode (0.51 ± 0.03 mA cm^{-2}). Table 1 summarizes microbial electrocatalytic performance with different bioelectrodes reported in previous works. To the best of our knowledge, the aforementioned maximum current density is the highest recorded to date with two-dimensional electrodes (composed of plane structures with identical surface morphology and property), such as pyrolytic carbon-SS felt (3.65 mA cm^{-2}) and self-assembled rGO (3.00 mA cm^{-2}). More detailed comparisons are provided in Table S2. The high microbial electrocatalytic performance is attributed to the open structure, high conductivity and large surface area of the rGO@PPy electrode. Porous electrode materials with large surface area are advantageous, because they can accommodate more cells inside the pores, which significantly enhances the current density. When feeding with sodium acetate was repeated, similar current values were recorded (Fig. 4a). As shown in Fig. 4b, current production started at 0.2 d (4.8 h) with the rGO@PPy electrode, whereas with the rGO and bare electrodes required about 1.1 d (26.4 h), suggesting that the startup time was much shorter with the hybrid electrode. When sodium acetate was consumed, LSV curves were obtained at a scan rate of 10 mV s^{-1} (Fig. 4c). The onset potential of the rGO@PPy electrode was much more negative than that of the rGO and bare electrodes and the current density of the rGO@PPy electrode was much higher than that of the rGO and bare electrodes, which is in accordance with the chronoamperometric data. CV curves for rGO@PPy, rGO and bare GCE bioelectrodes were also obtained (Fig. S7), and the results are in accordance with the conclusion based on the LSV results. *In situ* EIS

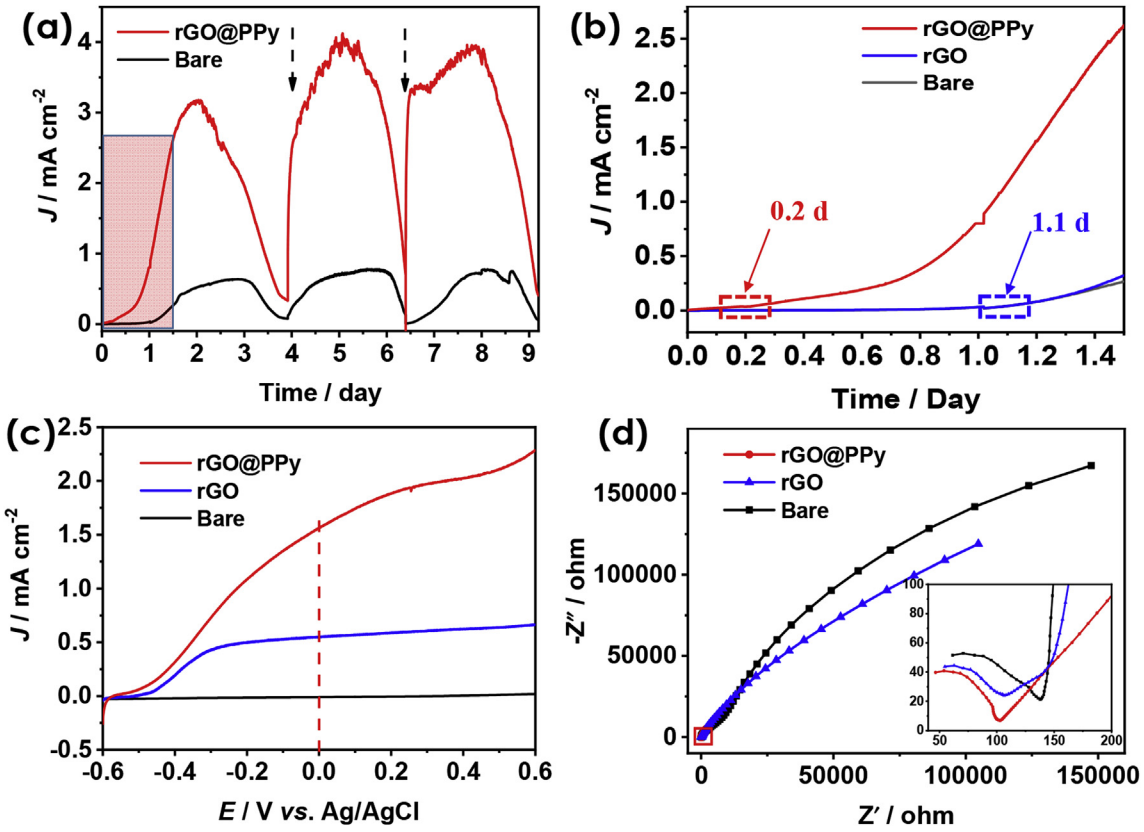

Figure 4. (a) Variation of current density over time for rGO@PPy and control bioelectrodes polarized at 0 V *vs.* saturated Ag/AgCl (arrows indicate feeding of 1.0 g L^{-1} sodium acetate); (b) The enlarged drawing of (a) between 0 and 1.5 day marked in a red box; (c) LSV curves for rGO@PPy, rGO and bare GCE bioelectrodes at a scan rate of 10 mV s^{-1}; (d) Nyquist plots for different bioelectrodes measured over a frequency range of 0.01–100000 Hz with an AC perturbation of 5 mV at 0 V *vs.* saturated Ag/AgCl. The inset is a magnification of the high frequency region, red square.

measurements in the bioreactor were conducted, and the Nyquist plots with different bioelectrodes are shown in Fig. 4d. The semi-diameter of the plot with the rGO@PPy electrode was much smaller than that with the rGO and bare electrodes. The rGO@PPy hybrid may provide a better physical contact to the bacteria cell surface and intimate contact with cell membranes might enormously facilitate direct-contact-based EET.

Table 1
Summary of BESs performance with different electrode materials.

Electrodes	J^{a} (mA cm^{-2})	Inoculum	Substrate	Ref.
Heat-treated SS felt	1.50	Anodic effluent	2 g/L acetate	[Guo et al., 2015]
Chitosan/vacuum stripped graphene	2.55	*P. aeruginosa*	5 g/L glucose	[He et al., 2012]
Biogenic Pd NPs	1.40	*S. oneidensis*	1.0 M formate	[Quan et al., 2015]
3D graphene/Pt	0.30	*S. oneidensis* MR-1	18 mM lactate	[Zhao et al., 2015]
CNT-textile	0.72	Domestic wastewater	1 g/L glucose	[Xie et al., 2010]
Microbially reduced-rGO	0.58	Anaerobic sludge	1 g/L acetate	[Yuan et al., 2012]
Self-assembled rGO	3.00	*S. oneidensis* MR-1	18 mM lactate	[Yong et al., 2014]
Pyrolytic carbon-SS felt	3.65	Anodic effluent	2 g/L acetate	[Guo et al., 2016]
PANI-graphene	0.45	*S. oneidensis* MR-1	18 mM lactate	[Yong et al., 2012]
FeS_2/rGO	1.10	*WWTPs*	2 g/L acetate	[Wang et al., 2018]
3D printed porous carbon	0.18	*S. oneidensis* MR-1	18 mM lactate	[Bian et al., 2018]
Electrospinning carbon fiber mat	3.00	Wastewater	10 mM acetate	[Chen et al., 2011]
N-doped CNT	0.63	Wastewater	1 g/L acetate	[Ci et al., 2012]
Ionic liquid-CNT	0.50	*S. putrefaciens* CN32	18 mM lactate	[Wei et al., 2016]
Layered corrugated carbon	1.44 ± 0.10	Wastewater	20 mM acetate	[Chen et al., 2012]
Carbon cloth	419[b]	Real wastewaters	Real wastewaters	[Pant et al., 2016]
PAN-GR	0.16 ± 0.01	*S. oneidensis* MR-1	18 mM lactate	[Patil et al., 2013]
PPy array	0.28	Wastewater	50 mM glucose	[Wang et al., 2016]
rGO@PPy	4.10 ± 0.02[c]	*G. sulfurreducens*	1 g/L acetate	This work

Notes: $n = 3$.
Abbreviations: SS, stainless steel; NPs, nanoparticles; CNT, carbon nanotubes; PANI, polyaniline; WWTPs, wastewater treatment plants; PAN-GR, electrospun carbon nanofibers obtained from polyacrylonitrile (PAN) blends with graphite.
[a] All the current densities were normalized to projected areas.
[b] In mW m^{-2}.
[c] Mean ± standard deviation.

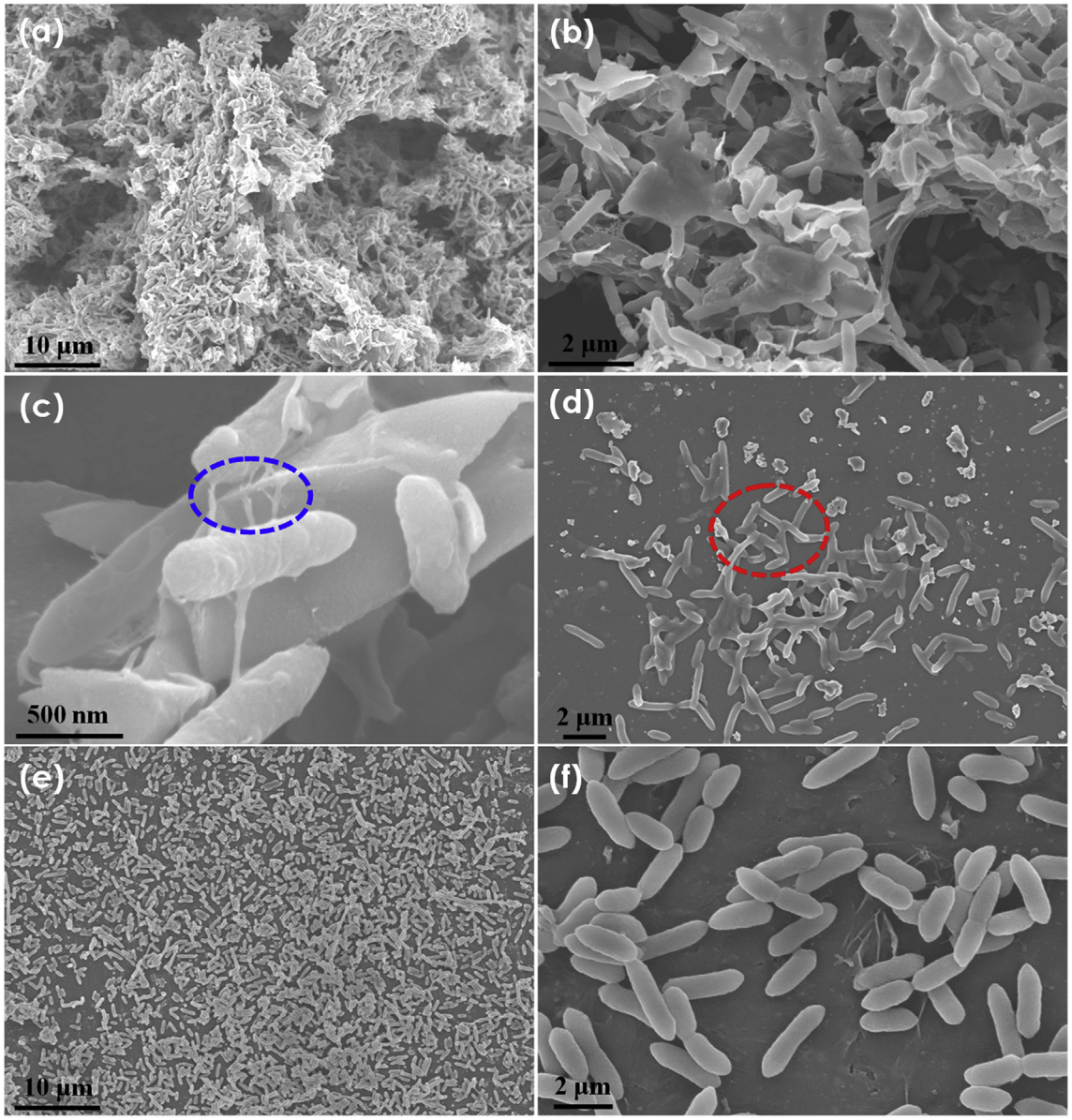

Fig. 5. SEM images of the microbial growth on different materials: (a, b, c) rGO@PPy, (d) PPy and (e, f) rGO.

3.4. Biofilm morphology

To better explain the superior performance of the rGO@PPy bioelectrode, the surface morphologies of the different bioelectrodes after 9 days of biofilm development were characterized by SEM. As seen in Fig. 5a and b, *Geobacter* cells adhered on the scaffold of the rGO@PPy electrode to form an interconnecting and thick biofilm network, suggesting a favorable structure for *Geobacter* colonization and growth. SEM images at high magnification (Fig. 5c) show many microbial nanowires (or pili) tethered cells to each other to form a stable multilayered network. Nanowires (pili) have been recognized as conductive bridges between exoelectrogens and electrode materials [Lovley et al., 2011; Pankratova et al., 2017; Ordonez et al., 2016]. In contrast, with the PPy and rGO modified electrodes, a low density bacterial biofilm was observed (Fig. 5d, e and f) due to the inherent flat structure of rGO and PPy. Additionally, much fewer biofilm pili were observed on the rGO and PPy electrode compared to those on the rGO@PPy electrode. Thus, the bacterial loading capacity of the rGO@PPy electrode is much higher than that of the PPy and rGO electrodes. Specifically, we estimated the bacterial area density on the interior surface of the rGO, PPy and rGO@PPy electrodes based on the SEM images and the following equation: $\rho = 10^6 \times N/A$ where ρ is the bacterial area density (cells mm^{-2}); N is the number of bacterial cells shown in corresponding SEM images; and A, is the area shown in corresponding SEM images estimated using the scale bars (μm^2) [Yang et al., 2016]. The bacterial areal density on the interior surface of rGO@PPy was estimated as 19500 ± 20 cells mm^{-2}, which is much larger than that of rGO (156 ± 12 cells mm^{-2}) and PPy (180 ± 15 cells mm^{-2}). These results demonstrate that the rGO@PPy electrode scaffold with a much higher accessible surface area is beneficial for biofilm growth and formation of nanowires, favoring EET, and thus resulting in higher power density.

In addition, the live-dead stained assay was used to evaluate bacteria viability on the rGO@PPy and rGO electrodes. The rGO@PPy after incubation with bacteria for different times was crushed into small pieces, rinsed with PBS, and stained with calcein AM (Invitrogen) and PI (Invitrogen), respectively. The live-dead stained assay revealed that almost all microorganisms were live (Fig. 6a and b), strongly suggesting that the good biocompatibility of the 3D macroporous architecture contributes to the excellent performance of the rGO@PPy electrode for electricity harvesting. The total protein content on different electrodes

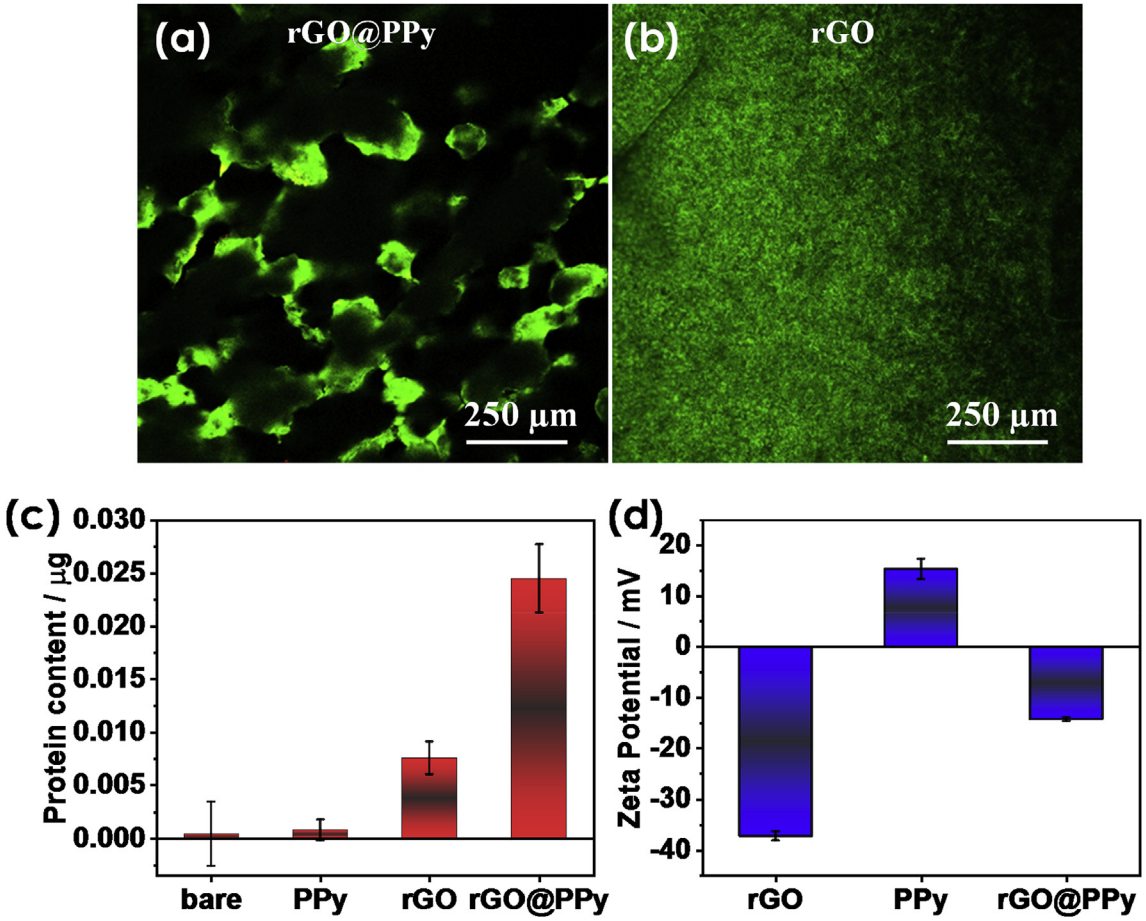

Fig. 6. CLSM images of the *Geobacter* cells on different electrodes (a, rGO@PPy; b, rGO) obtained after the output current during incubation was stable; (c) Total protein content on different electrodes; (d) Zeta potential of different electrodes. Error bars represent mean values ± one standard deviation, $n = 3$.

is shown in Fig. 6c. The total protein content on the rGO@PPy electrode was much higher than that on the bare PPy and rGO electrodes, which also reflects the great enhancement of biomass growth on the nanostructured rGO@PPy compared to unmodified GCE. From the Zeta potential data (Fig. 6d), it is noted that the rGO@PPy hybrids have a more positive surface charge than the bare PPy and rGO electrodes. As the surface charge of bacterial cells is negative, the more positively charged electrode surface enhances cell adhesion and biofilm formation [Guo et al., 2013].

4. Conclusions

In summary, we demonstrated the preparation of hierarchically nanostructured polypyrrole-reduced graphene oxide (rGO@PPy) hybrid electrode for enhancing microbial electrocatalysis. The open macroscale porous rGO@PPy structure provides a large specific surface area with rGO nanosheets as electron "highways", and the thin PPy coating improves electrode biocompatibility. The maximum current density of the rGO@PPy-*Geobacter sulfurreducens* bioelectrode could reach $4.10 \pm 0.02\,mA\,cm^{-2}$, which is 8-fold higher than that of bare rGO ($0.51 \pm 0.03\,mA\,cm^{-2}$), and is among the best performance recorded to date with two-dimensional electrodes. The result is ascribed to the optimum size matching of hierarchical pore structures, high conductivity and good biocompatibility, which facilitate microbial attachment and EET. The synergistic effect from rGO "e-bridge" and PPy surface affinity was designed to boost bioelectrocatalysis. This work provides a new insight for bioelectrode design and fabrication for their use in bioelectrochemical systems.

Declaration of interests

The authors declare that they have no known competing financial interests or personal relationships that could have appeared to influence the work reported in this paper.

CRediT authorship contribution statement

Liming Yang: Conceptualization, Formal analysis, Writing - original draft. **Genping Yi:** Formal analysis. **Yanan Hou:** Formal analysis, Writing - review & editing. **Haoyi Cheng:** Conceptualization, Formal analysis, Writing - review & editing. **Xubiao Luo:** Conceptualization, Writing - review & editing. **Spyros G. Pavlostathis:** Writing - review & editing. **Shenglian Luo:** Conceptualization, Writing - review & editing. **Aijie Wang:** Conceptualization, Writing - review & editing.

Acknowledgement

This work was supported by the National Natural Science Foundation of China (Grant No. 51808279), the National Key R&D Program of China (2018YFC0406400), the Department of Education Fund of Jiangxi Province (Grant No. GJJ170616), the Open Project of Key Laboratory of Environmental Biotechnology, CAS (Grant No. kf2018009), and Doctoral Scientific Research Foundation of Nanchang Hangkong University, Jiangxi Province (Grant No. EA201702384).

Appendix A. Supplementary data

Supplementary data to this article can be found online at https://

doi.org/10.1016/j.bios.2019.111444.

References

Aryal, N., Ammam, F., Patil, S.A., Pant, D., 2017. Green Chem. 19, 5748–5760.
Bian, B., Shi, D., Cai, X.B., Hu, M.J., Guo, Q.Q., Zhang, C.H., Wang, Q., Sun, X.A., Yang, J., 2018. Nanomater. Energy 44, 174–180.
Chaudhuri, S.K., Lovley, D.R., 2003. Nat. Biotechnol. 21, 1229–1232.
Chen, J., Deng, F., Hu, Y.Y., Sun, J., Yang, Y.G., 2015. J. Power Sources 290, 80–86.
Chen, S.L., Hou, H., Harnisch, F., Patil, S.A., Carmona-Martinez, A.A., Agarwal, S., Schröder, U., 2011. Energy Environ. Sci. 4, 1417–1421.
Chen, S.L., He, G.H., Liu, Q., Harnisch, F., Zhou, Y., Chen, Y., Hanif, M., Wang, S.Q., Peng, X.W., Hou, H.Q., Schröder, U., 2012. Energy Environ. Sci. 5, 9769–9772.
Ci, S.Q., Wen, Z.H., Chen, J.H., He, Z., 2012. Electrochem. Commun. 14, 71–74.
Cui, D., Yang, L.M., Liu, W.Z., Cui, M.H., Cai, W.W., Wang, A.J., 2018. J. Hazard Mater. 354, 244–249.
Ding, Y.B., Tang, Y.H., Yang, L.M., Zeng, Y.X., Yuan, J.L., Liu, T., Zhang, S.Q., Liu, C.B., Luo, S.L., 2016. J. Mater. Chem. 4, 14307–14315.
ElMekawy, A., Hegab, H.M., Losic, D., Saint, C.P., Pant, D., 2017. Renew. Sustain. Energy Rev. 72, 1389–1403.
Guo, K., Soeriyadi, A.H., Feng, H.J., Prevoteau, A., Patil, S.A., Gooding, J.J., Rabaey, K., 2015. Bioresour. Technol. 195, 46–50.
Guo, K., Freguia, S., Dennis, P.G., Chen, X., Donose, B.C., Keller, J., Gooding, J.J., Rabaey, K., 2013. Environ. Sci. Tech. 47, 7563–7570.
Guo, K., Hidalgo, D., Tommasi, T., Rabaey, K., 2016. Bioresour. Technol. 211, 664–668.
He, Z., Liu, J., Qiao, Y., Li, C.M., Tan, T.T.Y., 2012. Nano Lett. 12, 4738–4741.
Hochbaum, A.I., Aizenberg, J., 2010. Nano Lett. 10, 3717–3721.
Hou, J.X., Liu, Z.L., Zhang, P.Y., 2013. J. Power Sources 224, 139–144.
Hou, Y.N., Liu, H., Han, J.L., Cai, W.W., Zhou, J.Z., Wang, A.J., Cheng, H.Y., 2016. ACS Sustain. Chem. Eng. 4, 5392–5397.
Jiang, H.M., Yang, L., Deng, W.F., Tan, Y.M., Xie, Q.J., 2017. J. Power Sources 363, 27–33.
Katuri, K.P., Kalathil, S., Ragab, A., Bian, B., Alqahtani, M.F., Pant, D., Saikaly, P.E., 2018. Adv. Mater. 30, 1707072.
Kumar, R., Singh, L., Zularisam, A.W., 2016. Renew. Sustain. Energy Rev. 56, 1322–1336.
Kumar, A., Hsu, L.H.H., Kavanagh, P., Barrière, F., Lens, P.N.L., Lapinsonnière, L., Lienhard, V.J.H., Schröder, U., Jiang, X.C., Leech, D., 2017. Nat. Rev. Chem. 1, 0024.
Li, S., Cheng, C., Thomas, A., 2017. Adv. Mater. 29, 1602547.
Li, D.B., Huang, Y.X., Li, J., Li, L.L., Tian, L.J., Yu, H.Q., 2017. Electrochim. Acta 225, 452–457.
Liang, B., Ma, J.C., Cai, W.W., Li, Z.L., Liu, W.Z., Qi, M.Y., Zhao, Y.K., Ma, X.D., Deng, Y., Wang, A.J., Zhou, J.Z., 2019. Water Res. 148, 398–406.
Lin, T.Q., Chen, I.W., Liu, F.X., Yang, C.Y., Bi, H., Xu, F.F., Huang, F.Q., 2015. Science 350, 1508–1513.
Liu, C.B., Wang, K., Luo, S.L., Tang, Y.H., Chen, L.Y., 2011. Small 7, 1203–1206.
Liu, J., Qiao, Y., Guo, C.X., Lim, S., Song, H., Li, C.M., 2012. Bioresour. Technol. 114, 275–280.
Liu, S., Wang, F., Dong, R., Zhang, T., Zhang, J., Zheng, Z., Mai, Y., Feng, X., 2017. Small 13, 1604099.
Logan, B.E., Hamelers, B., Rozendal, R., Schröder, U., Keller, J., Freguia, S., Aelterman, P., Verstraete, W., Rabaey, K., 2006. Environ. Sci. Tech. 40, 5181–5192.
Logan, B.E., Rabaey, K., 2012. Science 337, 686–690.
Lovley, D.R., 2011. Energy Environ. Sci. 4, 4896–4906.
Mashkour, M., Rahimnejad, M., Pourali, S.M., Ezoji, H., ElMekawy, A., Pant, D., 2017. Prog. Nat. Sci-Mater 27, 647–651.
Massazza, D., Busalmen, J.P., Parra, R., Romeo, H.E., 2018. J. Mater. Chem. 6, 10019–10027.
Min, X.Y., Wu, X., Shao, P.H., Ren, Z., Ding, L., Luo, X.B., 2019. Chem. Eng. J. 358, 321–330.
Ordonez, M.V., Schrott, G.D., Massazza, D.A., Busalmen, J.P., 2016. Energy Environ. Sci. 9, 2677–2681.
Pant, D., Bogaert, G.V., Alvarez-Gallego, Y., Diels, L., Vanbroekhoven, K., 2016. Environ. Eng. Manag. J. 15, 1897–1904.
Pankratova, G., Gorton, L., 2017. Curr. Opin. Electrochem. 5, 193–202.
Patil, S.A., Chigome, S., Hägerhäll, C., Torto, N., Gorton, L., 2013. Bioresour. Technol. 132, 121–126.
Quan, X., Sun, B., Xu, H., 2015. Electrochim. Acta 182, 815–820.
Reguera, G., McCarthy, K.D., Mehta, T., Nicoll, J.S., Tuominen, M.T., Lovley, D.R., 2005. Nature 435, 1098–1101.
Ren, Y., Wang, J., Huang, X., Ding, J., 2015. Electrochim. Acta 186, 345–352.
Shao, P.H., Tian, J.Y., Duan, X., Yang, Y., Shi, W., Luo, X.B., Cui, F.Y., Luo, S., Wang, S.B., 2019. Chem. Eng. J. 359, 79–87.
Song, R.B., Zhao, C.E., Jiang, L.P., Abdel-Halim, E.S., Zhang, J.R., Zhu, J.J., 2016. ACS Appl. Mater. Interfaces 8, 16170–16177.
Song, R.B., Wu, Y.C., Lin, Z.Q., Xie, J., Tan, C.H., Loo, J.S.C., Cao, B., Zhang, J.R., Zhu, J.J., Zhang, Q.C., 2017. Angew. Chem. Int. Ed. 56, 10516–10520.
Sun, M., Zhai, L.F., Li, W.W., Yu, H.Q., 2016. Chem. Soc. Rev. 45, 2847–2870.
Tao, Y., Liu, Q., Chen, J., Wang, B., Wang, Y., Liu, K., Li, M., Jiang, H., Lu, Z., Wang, D., 2016. Environ. Sci. Tech. 50, 7889–7895.
Wang, R.W., Yan, M., Li, H.D., Zhang, L., Peng, B.Q., Sun, J.Z., Liu, D., Liu, S.Q., 2018. Adv. Mater. 30, 1800618.
Wang, W., You, S.J., Gong, X., Qi, D., Chandran, B.K., Bi, L., Cui, F.Y., Chen, X.D., 2016. Adv. Mater. 28, 270–275.
Wei, H., Wu, X.S., Zou, L., Wen, G.Y., Liu, D.Y., Qiao, Y., 2016. J. Power Sources 315, 192–198.
Xie, X., Criddle, C., Cui, Y., 2015. Energy Environ. Sci. 8, 3418–3441.
Xie, X., Hu, L.B., Pasta, M., Wells, G.F., Kong, D.S., Criddle, C.S., Cui, Y., 2010. Nano Lett. 11, 291–296.
Yang, L., Yan, D.F., Liu, C.B., Song, H.J., Tang, Y.H., Luo, S., Liu, M.J., 2015. J. Power Sources 278, 725–732.
Yang, L.M., Tang, Y., Luo, S.L., Liu, C., Song, H., Yan, D., 2014. ChemSusChem 7, 2907–2913.
Yang, L., Chen, Z.L., Cui, D., Luo, X.B., Liang, B., Yang, L.X., Liu, T., Wang, A.J., Luo, S.L., 2019. Chem. Eng. J. 359, 894–901.
Yang, L.M., Tang, Y., Yan, D.F., Liu, T., Liu, C.B., Luo, S., 2015. ACS Appl. Mater. Interfaces 8, 169–176.
Yang, Y., Liu, T., Zhu, X., Zhang, F., Ye, D., Liao, Q., Li, Y., 2016. Adv. Sci. 3, 1600097.
Ye, Z., Ellis, M.W., Nain, A.S., Behkam, B., 2017. J. Power Sources 347, 270–276.
Yong, Y.C., Yu, Y.Y., Zhang, X., Song, H., 2014. Angew. Chem. Int. Ed. 53, 4480–4483.
Yong, Y.C., Dong, X.C., Chan-Park, M.B., Song, H., Chen, P., 2012. ACS Nano 6, 2394–2400.
You, S.J., Ma, M., Wang, W., Qi, D.P., Chen, X.D., Qu, J.H., Ren, N.Q., 2016. Adv. Energy Mater. 7, 1601364.
Yu, H.Y., Shao, P.H., Fang, L.L., Pei, J.J., Ding, L., Pavlostathis, S.G., Luo, X.B., 2019. Chem. Eng. J. 359, 176–185.
Yuan, H.Y., He, Z., 2015. Nanoscale 7, 7022–7029.
Yuan, Y., Zhou, S., Zhao, B., Zhuang, L., Wang, Y., 2012. Bioresour. Technol. 116, 453–458.
Zhang, C.Y., Liang, P., Yang, X.F., Jiang, Y., Bian, Y.H., Chen, C.M., Zhang, X.Y., Huang, X., 2016. Biosens. Bioelectron. 81, 32–38.
Zhao, F., Slade, R.C.T., Varcoe, J.R., 2009. Chem. Soc. Rev. 38, 1926–1939.
Zhao, S.L., Li, Y.C., Yin, H.J., Liu, Z.Z., Luan, E.X., Zhao, F., Tang, Z.Y., Liu, S.Q., 2015. Sci. Adv. 1, 1500372.
Zou, L., Lu, Z.S., Huang, Y.H., Long, Z.E., Qiao, Y., 2017. J. Power Sources 359, 549–555.